MITSUBISHI ELECTRIC RESEARCH LABORATORIES
https://www.merl.com

Effect of Coil Geometry on Sensitivity Distribution in Field-Free Line Magnetic Particle Imaging

Washino, Masaomi; Lin, Chungwei; Matsuda, Tetsuya; Seino, Satoshi; Nakagawa, Takashi; Kiwa, Toshihiko

TR2026-115 August 07, 2026

Abstract

Magnetic particle imaging (MPI) with a field-free line (FFL) enables high-sensitivity visualization based on the nonlinear magnetization response of superparamagnetic nanoparticles. However, the superposition of the selection and drive fields modifies the local effective field and causes spatial variations in the system function. This paper presents a comparative analysis of two coil geometries: coaxial configuration (Co-Config.) and orthogonal configuration (Ortho-Config.), in which the drive-field direction is aligned with the FFL and perpendicular, respectively. Numerical simulations and experimental measurements showed that Co-Config. suppressed the polarity inversion and maintained a more uniform system function to enable stable single-harmonic detection. Conversely, Ortho-Config. produced sharper spatial variation together with polarity inversion in the system function. In the present third-harmonic reconstruction experiment, these sign-changing features appeared as localized reductions in reconstructed signal amplitude. These results show that the two coil geometries provide distinct native system-function characteristics, which should be considered when selecting the acquisition and reconstruction strategy for FFL-MPI systems.

Scientific Report 2026

© 2026 MERL. This work may not be copied or reproduced in whole or in part for any commercial purpose. Permission to copy in whole or in part without payment of fee is granted for nonprofit educational and research purposes provided that all such whole or partial copies include the following: a notice that such copying is by permission of Mitsubishi Electric Research Laboratories, Inc.; an acknowledgment of the authors and individual contributions to the work; and all applicable portions of the copyright notice. Copying, reproduction, or republishing for any other purpose shall require a license with payment of fee to Mitsubishi Electric Research Laboratories, Inc. All rights reserved.

Mitsubishi Electric Research Laboratories, Inc.
201 Broadway, Cambridge, Massachusetts 02139

Effect of Coil Geometry on Sensitivity Distribution in Field-Free Line Magnetic Particle Imaging

Masaomi Washino[1,3*], Chungwei Lin[2], Tetsuya Matsuda[1], Satoshi Seino[3], Takashi Nakagawa[3] and Toshihiko Kiwa[4]

[1] Mitsubishi Electric Corporation, 8-1-1 Tsukaguchi-Honmachi, Amagasaki, Hyogo 661-8661, Japan
[2] Mitsubishi Electric Research Laboratories, 201 Broadway, Cambridge, MA 02139-1955, USA
[3] The University of Osaka, 2-1 Yamadaoka, Suita, Osaka 565-0871, Japan
[4] Okayama University, 1-1-1 Tsushimanaka, Kita-ku, Okayama 700-0082, Japan
Correspondence to: Masaomi Washino (Washino.Masaomi@ap.MitsubishiElectric.co.jp)

Abstract

Magnetic particle imaging (MPI) with a field-free line (FFL) enables high-sensitivity visualization based on the nonlinear magnetization response of superparamagnetic nanoparticles. However, the superposition of the selection and drive fields modifies the local effective field and causes spatial variations in the system function. This paper presents a comparative analysis of two coil geometries: coaxial configuration (Co-Config.) and orthogonal configuration (Ortho-Config.), in which the drive-field direction is aligned with the FFL and perpendicular, respectively. Numerical simulations and experimental measurements showed that Co-Config. suppressed the polarity inversion and maintained a more uniform system function to enable stable single-harmonic detection. Conversely, Ortho-Config. produced sharper spatial variation together with polarity inversion in the system function. In the present third-harmonic reconstruction experiment, these sign-changing features appeared as localized reductions in reconstructed signal amplitude. These results show that the two coil geometries provide distinct native system-function characteristics, which should be considered when selecting the acquisition and reconstruction strategy for FFL-MPI systems.

1. Introduction

1.1 Overview of Magnetic Particle Imaging and Its Applications

Magnetic particle imaging (MPI) technology enables real-time and highly sensitive imaging using the nonlinear magnetization response of superparamagnetic iron oxide nanoparticles. Unlike X-ray computed tomography (CT), magnetic particle imaging (MPI) does not employ ionizing radiation. Similar to magnetic resonance imaging (MRI), MPI is a non-ionizing imaging modality; however, MPI directly detects the nonlinear magnetization response of magnetic nanoparticle tracers and can provide high-contrast tracer images without anatomical background signals [1], [2]. While MPI avoids ionizing radiation and reduces the procedural burden during longitudinal imaging, the safety profile

of repeated administration of magnetic nanoparticle (MNP) tracers depends on the particle formulation, surface coating, administered dose, biodistribution, and clearance pathway, and therefore remains an important consideration for future clinical translation [3]-[5].

Recent studies and reviews have demonstrated the potential of MPI in several actively developing biomedical applications, including cardiovascular imaging, cancer imaging, inflammation imaging, neuroimaging, and cell tracking [3], [4], [6]-[8]. Real-time in vivo blood-flow visualization has been demonstrated in early MPI studies [9]. Nanoparticle-enhanced tumor imaging and cancer-targeted MPI have been reported in both mechanistic and biological investigations [6], [7]. In addition, inflammation-related and immune-cell tracking applications have been discussed in recent biomedical MPI reviews [6], [10].

Preclinical studies have demonstrated high-contrast MPI tumor imaging using biologically targeted or functionalized MNPs, including applications in cancer detection and therapy monitoring [6], [7]. These results highlight the potential of MPI in oncology; however, such demonstrations rely on targeted or functionalized tracers rather than passive accumulation mechanisms.

1.2 Advantages of the Field-Free Line Method for Spatial Encoding

Spatial encoding in MPI is commonly classified into field-free point (FFP) and field-free line (FFL) approaches. These terms represent idealized descriptions of the low-field region used for spatial encoding. In practical scanners, MNPs located in the vicinity of the finite low-field region predominantly contribute to the measured signal, because particles outside this region are increasingly saturated by the selection field. The FFP method scans the imaging region by moving a point-like low-field region, whereas the FFL method scans a line-like low-field region across the region of interest [1]-[3], [11], [12]. Compared with FFP-based encoding, FFL-based encoding allows a larger low-field region to contribute to the measured signal, which can improve SNR. However, it also increases the complexity of spatial encoding and reconstruction, and projection-based, tomographic, or system-matrix-based reconstruction strategies have often been used for FFL-MPI [12]-[17].

In recent years, extensive research has been conducted on single-sided MPI, which leverages the benefits of the FFL method by arranging the magnetic-field generation coils on only one side of the system [15], [18]-[20]. Our research group is currently developing an MPI system based on the FFL method for the early diagnosis of Alzheimer's disease [21], [22]. We aim to develop a diagnostic agent that specifically binds to amyloid-β, a pathological hallmark of Alzheimer's disease, and deliver it directly to the brain via intranasal administration [23]. However, because brain uptake via the intranasal route is expected to be limited, high sensitivity to small quantities of MNPs is required for practical biomedical applications. The detection sensitivity and imaging performance of MPI systems have been investigated in previous studies on MPI system response, x-space reconstruction, system-matrix reconstruction, and FFL-based imaging [1]-[3], [11]-[14], [16]. The high sensitivity of the FFL

method presents considerable advantages and is expected to enhance the potential of MPI-based diagnostic technologies for practical applications.

1.3 Influence of Magnetic Field Superposition on the System Function in FFL-Based MPI

In the FFL method, image reconstruction is performed by recording the response of MNPs in the vicinity of the line-like low-field region generated by the selection field [12], [16], [24]. In MPI, the system function quantitatively describes the spatial response of nanoparticles and plays a central role in accurate image reconstruction [1] ,[11], [25]. Higher fidelity in the system function directly contributes to improved spatial resolution and image contrast [26], [27].

In FFL-based MPI, the selection and drive (alternating) fields must be jointly designed because their superposition determines the local effective magnetic field experienced by the nanoparticles [9], [28]. The selection magnetic field forms the FFL geometry and spatial gradient, while the drive field induces nonlinear magnetization dynamics and generates the detectable harmonic signals. The relative orientation of these two fields modifies the time derivative of the magnetic field, which in turn shapes the spatial characteristics of the system function.

In this study, two representative coil geometries are considered: the coaxial configuration (Co-Config.) in which the drive-field direction is aligned with the extension axis of the FFL, and the orthogonal configuration (Ortho-Config.) in which the drive-field direction is perpendicular to the FFL. These definitions are applied consistently throughout the manuscript.

Depending on whether the FFL and drive-field directions are aligned (coaxial) or perpendicular (orthogonal), the system function exhibits different spatial sensitivity patterns. In Ortho-Config., polarity inversion and sign-changing regions appear due to the spatial variation of the time-derivative field component. Under the single-harmonic acquisition and reconstruction conditions used in this study, these features can cause partial cancellation of opposite-polarity signal components and affect the reconstructed amplitude. However, when the full system function is explicitly incorporated into a more complete multi-harmonic or system–matrix reconstruction framework, the sharper spatial variation in Ortho-Config. may also provide useful high-spatial-frequency encoding information. In this study, only the third harmonic was used intentionally to emphasize the native hardware-induced differences between coil geometries before applying such advanced reconstruction frameworks. In contrast, Co-Config. maintains a single-polarity system function under the present measurement conditions, which provides a different spatial-response characteristic from Ortho-Config.

Previous FFL-MPI studies have investigated orthogonal or electronically rotated FFL configurations mainly for projection or tomographic imaging [16], [17]. In contrast, the present study focuses on the native system-function differences caused by the relative orientation of the FFL and drive field under a controlled single-harmonic acquisition condition. In this study, our objective is not to determine the optimal coil geometry but to compare, in a controlled manner, how coil configuration affects the native

system function. Section 2 presents the theoretical background and introduces the two coil geometries. Section 3 describes the experimental setup and imaging methodology. Section 4 analyzes the system function characteristics and their implications. Section 5 summarizes the findings and discusses future research directions.

2. Theory and Numerical Calculations

2.1 Theory of the System Function

The equations presented in this section follow established MPI theory as described by Gleich & Weizenecker [1], Goodwill & Conolly [2], Knopp & Buzug [11], Knopp et al. [14], Barış & Güngör [15], and Tonyushkin [19]. These standard formulations provide the theoretical basis for comparing the coaxial and orthogonal coil configurations examined in this study.

In MPI, the system function relates the nanoparticle distribution to the measured voltage and is the foundation for image reconstruction.

The signal measured by the receiver coil that detects the magnetization response of the nanoparticles is expressed as follows:

$$u_p(t) = \int d\boldsymbol{r}\, s(\boldsymbol{r},t)c(\boldsymbol{r}) \tag{2.1}$$

$$s(\boldsymbol{r},t) = -\mu_0 \boldsymbol{p}_R(\boldsymbol{r}) \cdot \frac{\partial \bar{\boldsymbol{m}}(\boldsymbol{r},t)}{\partial t} \tag{2.2}$$

where $c(\boldsymbol{r})$ denotes the distribution function of the MNPs and $s(\boldsymbol{r},t)$ denotes the system function in the time domain.

In addition, the receiver-coil sensitivity is represented by $\boldsymbol{p}_R(\boldsymbol{r})$, and the magnetic moment of the MNP ensemble is also represented by $\bar{\boldsymbol{m}}(\boldsymbol{r},t)$. The ensemble magnetic moment is defined as

$$\bar{\boldsymbol{m}}(\boldsymbol{r},t) = \frac{1}{N_P}\sum_{j=1}^{N_P} \boldsymbol{m}_j(\boldsymbol{r},t) \tag{2.3}$$

where $\boldsymbol{m}_j(\boldsymbol{r},t)$ is the magnetic moment vector of the j-th MNP, and N_P is the number of MNPs contributing to the local response. Since $\boldsymbol{p}_R(\boldsymbol{r})$ is completely determined by the receiver coil geometry, $\bar{\boldsymbol{m}}$ is dependent only on the magnetic properties of the nanoparticles and the external field $\bar{\boldsymbol{m}}(\boldsymbol{r},t) = \bar{m}(|\boldsymbol{H}(\boldsymbol{r},t)|,t)\hat{\boldsymbol{e}}_H(\boldsymbol{r},t)$. Substituting this into Equation (2.2), we obtain

$$s(\boldsymbol{r},t) = -\mu_0 \boldsymbol{p}_R(\boldsymbol{r}) \cdot \frac{\partial \bar{m}(|\boldsymbol{H}(\boldsymbol{r},t)|,t)\hat{\boldsymbol{e}}_H(\boldsymbol{r},t)}{\partial t} \tag{2.4}$$

The k-th harmonic component of the system function in the frequency domain $\hat{s}_k(\boldsymbol{r})$ can be obtained by taking the Fourier transform of Equation (2.2) as follows:

$$\hat{s}_k(\boldsymbol{r}) = \frac{1}{T_R}\int_0^{T_R} dt\, s(\boldsymbol{r},t)e^{-2\pi ikt/T_R} \tag{2.5}$$

$$= -\frac{\mu_0}{T_R}\int_0^{T_R} dt\, \boldsymbol{p}_R(\boldsymbol{r})\cdot\frac{\partial\bar{\boldsymbol{m}}(\boldsymbol{r},t)}{\partial t}e^{-2\pi ikt/T_R} \tag{2.6}$$

where T_R denotes the period of the fundamental frequency of the alternating drive field.

Because the saturation magnetic moment of the nanoparticles is denoted by $\bar{m}_S$, the average magnetic moment under magnetic field B is given as

$$\bar{m}(B) = \frac{\int_{-1}^{1} dx\,(\bar{m}_S x)e^{-B\bar{m}_S x/(k_B T_P)}}{\int_{-1}^{1} dx\, e^{-B\bar{m}_S x/(k_B T_P)}} = \bar{m}_S\mathcal{L}(\beta_B B) \tag{2.7}$$

where $\mathcal{L}(x) = \coth(x) - 1/x$ denotes the Langevin function, T_P denotes the temperature of MNPs, k_B denotes the Boltzmann constant, and $\beta_B = \bar{m}_S/(k_B T_P)$.

Using the relation $B = \mu_0 H$, the expression can also be rewritten as

$$\bar{m}(H) = \bar{m}_S\mathcal{L}(\beta H) = \bar{m}_S\mathcal{L}(\beta_B B) \tag{2.8}$$

$$\beta = \mu_0\frac{\bar{m}_S}{k_B T_P} = \mu_0\beta_B \tag{2.9}$$

2.2 Arrangement of the Selection-Field Generator, Drive Coil, and Receive Coil

In the FFL-based MPI framework, we considered two coil geometries for generating and detecting magnetic fields, as shown in Fig. 1. Co-Config. denotes the configuration in which the drive-field direction is aligned with the extension direction of the FFL, while Ortho-Config. denotes the configuration in which these directions are orthogonal.

The FFL was generated by a pair of rectangular permanent magnets and U-shaped iron yokes arranged face-to-face. This permanent-magnet-based configuration belongs to the broader class of FFL-generation approaches reported in MPI, including electromagnetically generated FFLs, electronically rotated FFLs, single-sided FFL generators, and mechanically scanned FFL generators [12], [14]-[20], [28]. The FFL extended along the Z-axis, and the sample was scanned along the X-axis in both configurations. The alternating drive field was generated by a Helmholtz-type drive coil. In Co-Config., the drive field was applied along the Z-axis, parallel to the FFL. In Ortho-Config., the drive field was applied along the X-axis, perpendicular to the FFL. The magnetization response of the MNPs was detected by a gradiometer receive coil.

The interaction between the static selection field and the alternating drive field differs between the two geometries, resulting in distinct system-function characteristics and imposing different design constraints on allowable coil arrangements. These constraints significantly influence the signal

detection sensitivity and determine the appropriate signal processing strategies.

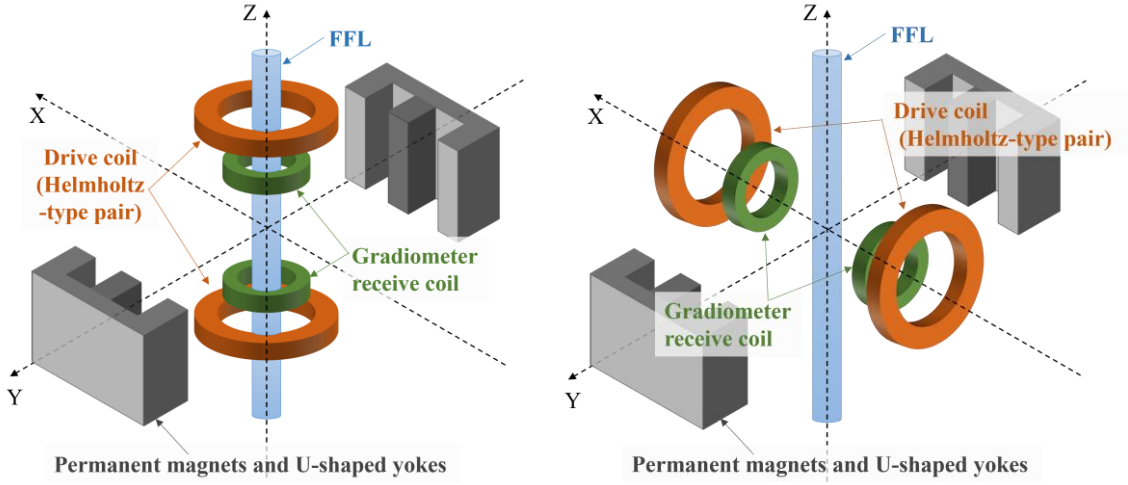

(a) Co-Config (b) Ortho-Config.

Figure 1. Conceptual geometries of the FFL generator and coil arrangement used in this study: (a) Co-Config. and (b) Ortho-Config. The FFL was generated by a pair of rectangular permanent magnets and U-shaped iron yokes arranged face-to-face and extended along the Z-axis. The sample was scanned along the X-axis in both configurations. The drive field was generated by a Helmholtz-type drive coil and was applied parallel to the FFL in Co-Config. and perpendicular to the FFL in Ortho-Config. The magnetization response was detected by a gradiometer receive coil.

2.3 System Function in Co-Config.

We consider the system function in Co-Config., where the extension direction of the FFL and the direction of the excitation magnetic field were both aligned along the Z-axis.

Assuming that the excitation magnetic field is applied along the Z-axis, it is represented as $\boldsymbol{H}_{\boldsymbol{drive}}^{(\boldsymbol{Z})} = (0, 0, A\cos\omega t)$. In the following analytical model, the selection field is approximated as an ideal linear field near the central region of the scanner in order to clarify the coil-geometry-dependent mechanism of the system function. If the magnetic field gradient of the FFL near the center is G T/m, the selection magnetic field is approximated as $\boldsymbol{H}_{\boldsymbol{Select}} = (-Gx, Gy, 0)$ [1], [2], [11]. Thus, the total magnetic field applied to MNPs $\boldsymbol{H}^{(z)}$ is defined as

$$\boldsymbol{H}^{(z)} = \boldsymbol{H}_{\boldsymbol{drive}}^{(\boldsymbol{Z})} + \boldsymbol{H}_{\boldsymbol{Select}} = \begin{bmatrix} -Gx \\ Gy \\ A\cos\omega t \end{bmatrix} \tag{2.10}$$

$$\left|\boldsymbol{H}^{(z)}\right| = \sqrt{G^2(x^2+y^2) + (A\cos\omega t)^2} \tag{2.11}$$

$$\hat{\boldsymbol{e}}_H^{(z)} = \frac{\boldsymbol{H}^{(z)}}{\left|\boldsymbol{H}^{(z)}\right|} \tag{2.12}$$

The average magnetic moment $\bar{\boldsymbol{m}}$ under the field $\boldsymbol{H}^{(z)}$ can be expressed using the Langevin function

as follows:

$$\bar{\boldsymbol{m}}(\boldsymbol{r},t) = \bar{m}(|\boldsymbol{H}(\boldsymbol{r},t)|,t)\hat{\boldsymbol{e}}_H(\boldsymbol{r},t) \tag{2.13}$$

where $\hat{\boldsymbol{e}}_H(\boldsymbol{r},t) = \boldsymbol{H}(\boldsymbol{r},t)/|\boldsymbol{H}(\boldsymbol{r},t)|$. Because the receive sensitivity in Co-Config. is directed along the Z-axis, the Z-component of the receive sensitivity is used in the projected system function. Thus, the system function can be described using Equations (2.5)–(2.7) and (2.10)–(2.12) as follows:

$$\begin{aligned} s^{(z)}(\boldsymbol{r},t) &= -\mu_0 p_{R,z}(\boldsymbol{r})\frac{\partial \bar{m}_z(\boldsymbol{r},t)}{\partial t} \\ &= -\mu_0 p_{R,z}(\boldsymbol{r})\frac{\partial \bar{m}\left(\left|\boldsymbol{H}^{(z)}(\boldsymbol{r},t)\right|,t\right)\hat{\boldsymbol{e}}_{H,z}^{(z)}(\boldsymbol{r},t)}{\partial t} \\ &= -\mu_0 p_{R,z}(\boldsymbol{r})\bar{m}_s\frac{\partial}{\partial t}\left[\frac{\mathcal{L}\left(\beta\sqrt{G^2(x^2+y^2)+(A\cos\omega\, t)^2}\right)A\cos\omega\, t}{\sqrt{G^2(x^2+y^2)+(A\cos\omega\, t)^2}}\right] \end{aligned} \tag{2.14}$$

The component $p_{R,z}(\boldsymbol{r})$ denotes the Z-direction component of the receive sensitivity. The frequency domain representation of the system function is given as

$$\hat{s}_k^{(z)}(\boldsymbol{r}) = \hat{s}_k^{(z)}(x,y) = \frac{1}{T_R}\int_0^{T_R} dt\, s^{(z)}(\boldsymbol{r},t)e^{-2\pi ikt/T_R} \tag{2.15}$$

where $\omega = 2\pi/T_R$. It can be observed that the system function is independent of the Z-direction and depends only on the distance from the FFL.

In the following numerical maps, the magnetization response was treated as instantaneous, and magnetic relaxation was not explicitly included. Therefore, Figs. 2 and 3 show the signed third-harmonic system-function component referenced to the drive field, rather than a relaxation-dependent magnitude-and-phase decomposition. The positive and negative regions indicate opposite-polarity components of the selected harmonic response.

Fig. 2 shows the numerically calculated two-dimensional distribution of the signed third-harmonic system-function component under the following conditions: $A = 16$ mT, $G = 2$ T/m, and excitation frequency of 500 Hz.

The receive-coil sensitivity used in the calculations was derived from the geometry and dimensions of the gradiometer receive coils described in Section 3.1 and shown in Figs. 4 and 5.

For example, we assumed Resovist® (FUJIFILM RI Pharma Co., Ltd.) with an iron concentration of 27.875 mg/mL and a core diameter of 28 nm.

Assuming that the MNPs consist of Fe_3O_4, the saturation magnetization M_S (magnetic moment per unit volume) is 4.77×10^5 A/m. Given a particle volume V, the saturation magnetic moment is calculated as $\bar{m}_S = VM_S$. The calculated component in Co-Config. retained the same polarity over the sensitive region, as shown in Fig. 2.

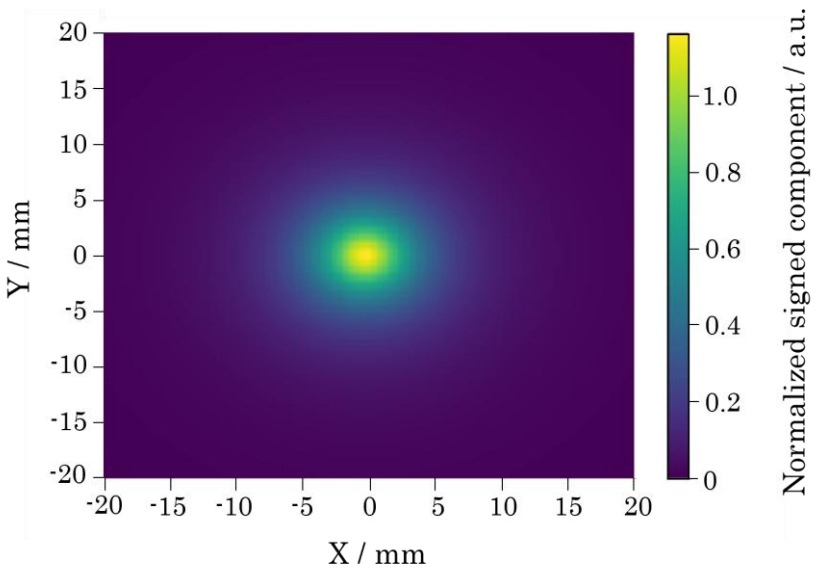

Figure 2. Two-dimensional distribution of the signed third-harmonic system-function component in Co-Config. for A = 16 mT and G = 2 T/m. The values are normalized by the maximum absolute value of the calculated component.

2.4 System Function in Ortho-Config.

Subsequently, we analyzed the system function in Ortho-Config., where the excitation magnetic field was perpendicular to the FFL extension direction.

When the drive field is applied along the X-direction, it is described as $\boldsymbol{H}_{\boldsymbol{drive}}^{(\boldsymbol{X})} = (A\cos\omega t, 0, 0)$. Similar to Co-Config., the selection field in Ortho-Config. is treated as an ideal linear approximation near the central region of the scanner. If the magnetic field gradient of the FFL near the center is given by G T/m, the selection magnetic field is approximated as $\boldsymbol{H}_{\boldsymbol{Select}} = (-Gx, Gy, 0)$ [1], [2], [11]. The total magnetic field applied to the MNPs $\boldsymbol{H}^{(x)}$ can be defined as

$$\boldsymbol{H}^{(x)} = \boldsymbol{H}_{\boldsymbol{drive}}^{(\boldsymbol{X})} + \boldsymbol{H}_{\boldsymbol{Select}} = \begin{bmatrix} -Gx + A\cos\omega t \\ Gy \\ 0 \end{bmatrix} \tag{2.16}$$

$$\left|\boldsymbol{H}^{(x)}\right| = \sqrt{G^2(x^2+y^2) + (A\cos\omega t)^2 - 2GAx\cos\omega t} \tag{2.17}$$

$$\hat{e}_H^{(x)} = \frac{\boldsymbol{H}^{(x)}}{|\boldsymbol{H}^{(x)}|} \tag{2.18}$$

Because the receive sensitivity in Ortho-Config. is directed along the X-axis, the X-component of the receive sensitivity is used in the projected system function. Thus, the system function is expressed using Equations (2.16)–(2.18) as follows:

$$s^{(x)}(\boldsymbol{r}, t) = -\mu_0 p_{R,x}(\boldsymbol{r}) \frac{\partial \overline{m}_x(\boldsymbol{r}, t)}{\partial t} \tag{2.19}$$

$$= -\mu_0 p_{R,x}(\boldsymbol{r}) \frac{\partial \bar{m}\left(\left|\boldsymbol{H}^{(x)}(\boldsymbol{r},t)\right|,t\right)\hat{e}_{H,x}^{(x)}(\boldsymbol{r},t)}{\partial t}$$

$$= -\mu_0 p_{R,x}(\boldsymbol{r})\bar{m}_S \frac{\partial}{\partial t}\left[\frac{\mathcal{L}\left(\beta\sqrt{G^2(x^2+y^2) + (A\ \cos\omega t)^2 - 2GAx\cos\omega t}\right)(-Gx +}{\sqrt{G^2(x^2+y^2) + (A\ \cos\omega t)^2 - 2GAx\cos\omega t}}\right.$$

The component $p_{R,x}(\boldsymbol{r})$ denotes the X-direction component of the receive sensitivity. The frequency-domain expression for the k-th harmonic of the system function is given by

$$\hat{s}_k^{(x)}(\boldsymbol{r}) = \hat{s}_k^{(x)}(x,y,z) = \frac{1}{T_R}\int_0^{T_R} s^{(x)}(\boldsymbol{r},t)e^{-2\pi ikt/T_R}\,dt \tag{2.20}$$

Similar to the Co-Config. case, the two-dimensional distribution of the signed third-harmonic system-function component was numerically calculated under the following conditions: $A = 16$ mT, $G = 2$ T/m, and excitation frequency of 500 Hz.

The results are shown in Fig. 3. Unlike the Co-Config. case, the calculated component in Ortho-Config. contained both positive and negative regions, indicating polarity reversal of the selected harmonic component.

In the context of the present single-harmonic reconstruction, this polarity inversion can cause partial cancellation of opposite-polarity signal components and affect the reconstructed amplitude. This behavior should be explicitly considered in the reconstruction model. In a more complete reconstruction framework that incorporates the full system function, the sign-changing profile may also provide additional spatial-encoding information.

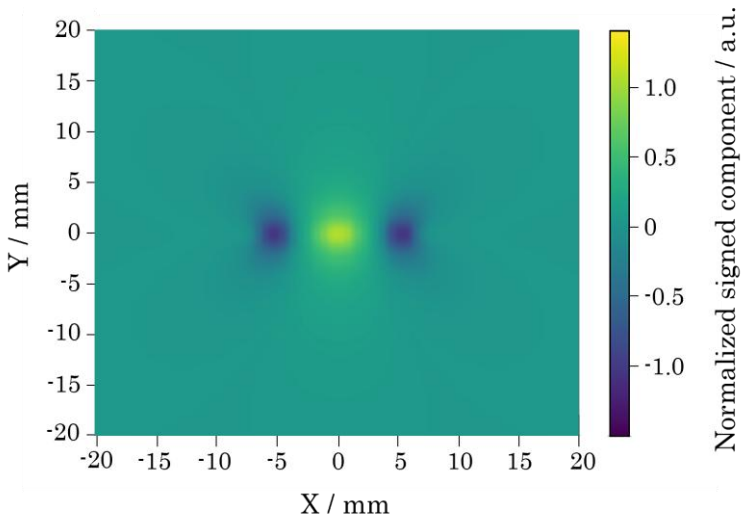

Figure 3. Two-dimensional distribution of the signed third-harmonic system-function component in Ortho-Config. for A = 16 mT and G = 2 T/m. Positive and negative regions indicate polarity reversal of the selected harmonic component. The values are normalized by the maximum absolute value of the calculated component.

2.5 Comparison of the System Functions between Co-Config. and Ortho-Config.

This section explains the mechanism underlying the generation of sign-changing regions by focusing on the differences in the time derivatives of the magnetic fields in Co-Config. and Ortho-Config.

The system functions in Co-Config. are described by Equation (2.14). Focusing on the time, the Langevin function $\mathcal{L}\left(\beta\sqrt{G^2(x^2+y^2)+(A\cos\omega\, t)^2}\right)$ represents the magnetization response of the MNPs. Thus, the time derivative of the remaining term $A\cos\omega\, t/\sqrt{G^2(x^2+y^2)+(A\cos\omega\, t)^2}$ reflects the time variation of the magnetic field. In this case, the polarity of the time derivative of the magnetic field depends on the time-varying term $A\cos\omega\, t\,\partial(A\cos\omega\, t)/\partial t = -A\omega\sin\omega\, t$. Essentially, the polarity of the time derivative depends only on the time, and not on the spatial position, and remains constant corresponding to the position.

Consequently, the polarity of the system function is spatially constant, and sign-changing regions do not occur in Co-Config. From a symmetry point of view, Equation (2.14) depends solely on $x^2 + y^2$ and not on x or y, ensuring the same polarity over the entire domain.

This spatially uniform polarity facilitates a stable interpretation of the single-harmonic system-function profile in Co-Config. and makes the measured sensitivity distribution easier to relate to the theoretical FFL geometry.

In contrast, the system function in Ortho-Config. is described by Equation (2.18). Considering the time derivative, the term $(-Gx + A\cos\omega\, t)/\sqrt{G^2(x^2+y^2) + (A\cos\omega t)^2 - 2GAx\cos\omega t}$ contributes to the time variation of the magnetic field.

In this case, the polarity of the time derivative depends on both t and the spatial coordinate x, particularly through the numerator $-Gx + A\cos\omega\, t$. In regions where $Gx \approx A\cos\omega\, t$ (i.e., near the center of the FFL), the time derivative approaches zero and the polarity changes. This polarity inversion in the time derivative reversed the polarity of the system function, causing the emergence of regions with opposite polarity.

In summary, the difference in the occurrence of sign-changing regions between Co-Config. and Ortho-Config. originates from the behavior of the time derivative of the magnetic field.

In Co-Config., the polarity of the time derivative is spatially constant under the present field geometry, resulting in a single-polarity system-function profile. In Ortho-Config., the polarity varies with spatial position, resulting in sign-changing regions in the selected harmonic component. These positive and negative regions correspond to opposite-polarity components under the present single-harmonic detection condition. The sharper spatial variation observed in Ortho-Config. represents a native system-function characteristic that may provide high-spatial-frequency encoding information when incorporated into an appropriate reconstruction framework, rather than direct evidence of inherently better spatial resolution.

3. Experimental Methods (Measurement of System Function and Cross-Sectional Imaging)

3.1 Description of the MPI System

In this section, we describe the MPI system used in the study.

Figs. 4 and 5 present the schematics and actual photographs of the MPI systems in Co-Config. and Ortho-Config., respectively. The MPI setups for both configurations can be constructed by replacing only the coil system, which consists of an excitation coil placed at the center and a detection coil (gradiometer coil).

To generate the FFL, we employed a configuration in which permanent magnets and U-shaped yokes were arranged face-to-face. Using this setup, the FFL was extended along the Z-axis and centered in the middle of the device. The use of permanent magnets and yokes enables the formation of a stable FFL for spatial encoding in MPI.

The sample position is controlled using a three-axis motion controller to enable translational movement along the X- and Y-directions and rotational movement (θ) around the X-axis. The main scanning direction was the X-axis for both Co-Config. and Ortho-Config. The same sample translation path and field of view (FOV) were used to ensure a fair comparison between the two coil geometries.

The magnetization signals from the MNPs were fed into a lock-in amplifier, and a current sensor (CT) placed at the output of the AC power supply (constant-current source) was used as a reference signal for synchronous detection. This method is suitable for the high-sensitivity detection of weak magnetization signals. No analog or digital filtering was applied. The lock-in amplifier selectively demodulated only the specified harmonic component (the third harmonic in this study), thus the fundamental drive-field frequency is neither detected nor used in the analysis.

For the drive field coil, a Helmholtz-type coil was used to ensure uniform magnetic field distribution within the FOV region.

A gradiometer receive coil was used for signal detection to suppress direct inductive coupling from the drive coil and spatially broad background pickup components. In Co-Config., a second-order gradiometer was used to suppress both uniform and approximately linear pickup components associated with the drive field and the magnet-based FFL environment. In contrast, Ortho-Config. employed a first-order gradiometer, which was sufficient to suppress the dominant uniform pickup component under the present receive-axis condition. The different gradiometer orders were selected to stabilize signal detection in each magnetic-field environment and were not intended to change the spatial encoding mechanism itself. Although the gradiometer in Co-Config. was oriented perpendicular to the XY-plane, its sensitive region was sufficiently wide for the sample to remain within the detection area throughout the X-axis translation. These choices ensured stable signal detection under the respective magnetic-field environments used in this study. The corresponding gradiometer coil arrangements are shown schematically in Figs. 4(a) and 5(a). Because the first- and

second-order gradiometers have different receive-sensitivity distributions, the absolute signal amplitudes obtained in the two configurations are affected by the receive-coil geometry. In the numerical calculation and reconstruction, the receive sensitivity corresponding to each coil geometry was used. Therefore, the comparison in this study focuses on the normalized system-function profiles, polarity behavior, and spatial-response patterns, rather than on an absolute comparison of receive sensitivity or SNR between the two gradiometer designs. No separate transfer-function correction was applied to the complete detection chain. The same current-reference and lock-in detection scheme was used for all measurements, and the measured profiles were normalized for comparison.

In Co-Config., the drive coil and gradiometer receive coil were aligned coaxially along the Z-axis, as shown in Fig. 4. Conversely, in Ortho-Config., the drive coil and gradiometer receive coil were aligned coaxially along the X-axis, as shown in Fig. 5. The coordinate system used in this study was explicitly defined to clarify these geometric relations.

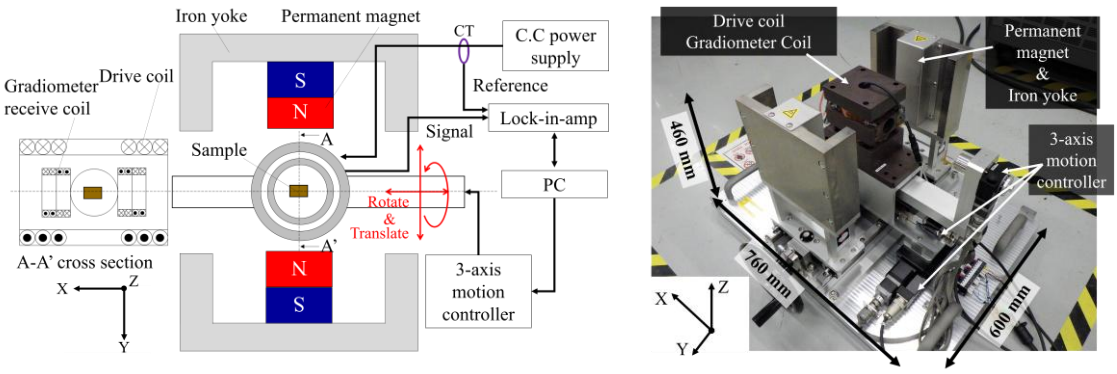

(a) Schematic diagram (b) Actual device

Figure 4. MPI device with Co-Config.: (a) schematic diagram and (b) photograph of the experimental setup. The coordinate axes in (b) were added to correspond to those in (a). The drive field was applied along the Z-axis, parallel to the FFL. The drive coil and gradiometer receive coil were aligned along the Z-axis, and the sample was translated along the X-axis during scanning. The overall system dimensions along the X-, Y-, and Z-directions were 760, 600, and 460 mm, respectively.

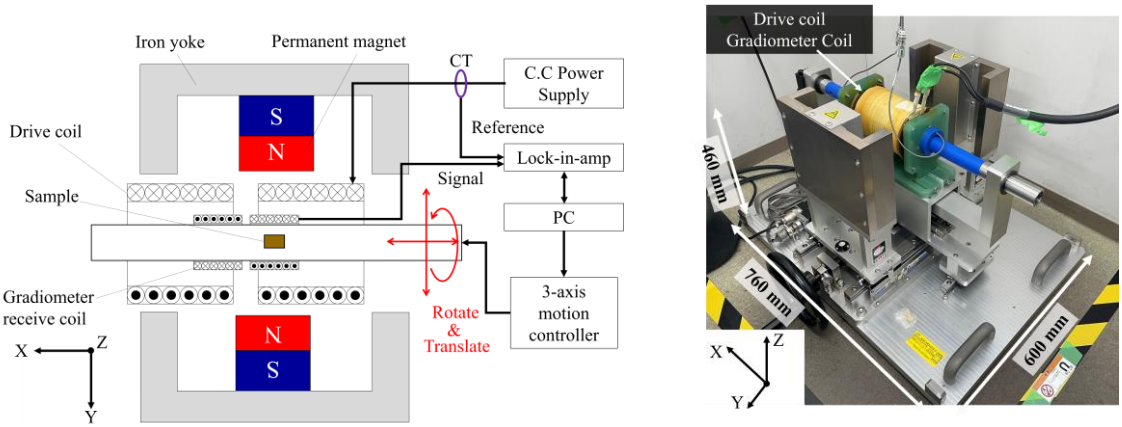

(a) Schematic diagram (b) Actual device

Figure 5. MPI device with Ortho-Config.: (a) schematic diagram and (b) photograph of the experimental setup. The coordinate axes in (b) were added to correspond to those in (a). The drive field was applied along the X-axis, perpendicular to the FFL. The drive coil and gradiometer receive coil were aligned along the X-axis, and the sample was translated along the X-axis during scanning. The overall system dimensions along the X-, Y-, and Z-directions were 760, 600, and 460 mm, respectively.

3.2 Measurement of One-Dimensional System Function

To experimentally evaluate the sensitivity distribution of the system function, we prepared a cylindrical sample with a diameter of 2 mm and length of 8 mm (corresponding to a MNP volume of 25.0 μL). The sample was scanned along the X-direction for both coil configurations. Fig. 6 shows a photograph of the sample. We used Resovist® (FUJIFILM Toyama Chemical Co., Ltd.) as the MNP material, which is clinically applied as an MRI contrast agent and widely studied in MPI applications. The sample was oriented along the Z-direction.

Although point-like samples are typically used to obtain ideal system functions, we employed a small-diameter cylindrical sample, considering realistic measurement constraints.

The measurements were performed under two selection-field gradient conditions: G = 1 T/m and G = 2 T/m. These values denote the achieved selection-field gradients evaluated near the central FFL region. The two gradient conditions were obtained by adjusting the distance between the facing permanent-magnet/yoke assemblies along the Y-direction, which corresponds to the gap direction of the FFL generator. The achieved gradients were confirmed from the measured magnetic-field distribution near the central FFL region.

The alternating drive field was set to a frequency of 500 Hz and an amplitude of 16 mT. Because this frequency is lower than the typical MPI drive-field range, we also measured the AC susceptibility spectrum of Resovist to verify whether nonlinear responses remained detectable at 500 Hz. The

measured χ' and χ'' spectra are shown in Fig. 7. Here, χ' denotes the in-phase component of the complex AC susceptibility, and χ'' denotes the out-of-phase component associated with magnetic relaxation loss. The in-phase component χ' maintains a sufficiently high magnitude at 500 Hz, while the out-of-phase component χ'' exhibits a nonzero value. Since χ'' is associated with magnetic relaxation loss and harmonic signal generation in MPI, these results confirm that higher-order harmonics—including the third harmonic used in this study—remain detectable at 500 Hz.

This verification supports the suitability of the 500 Hz drive-field setting used in this study. Because the primary objective is a controlled comparison between Co-Config. and Ortho-Config. under identical excitation conditions, and because low-frequency drive fields are relevant for future large-scale MPI systems with high-inductance coils, the use of 500 Hz is appropriate for system function evaluation.

During the scan, the sample was translated along the X- or Y-direction, and the magnetization response signal was measured at each position. The system function distributions along the X-axis (Y = 0) and Y-axis (X = 0) were then analyzed.

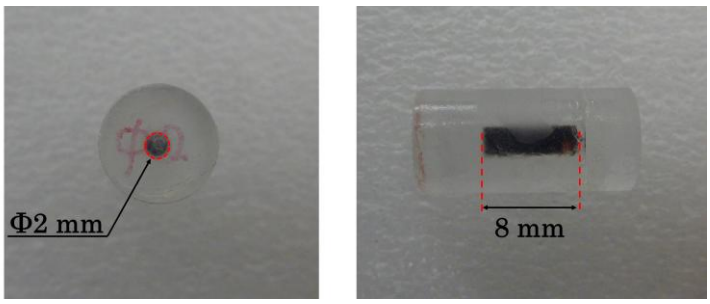

Figure 6. Photograph of the MNP sample (2-mm-diameter cylinder, 25.0 μL volume). The length of the nanoparticle sample is 8.0 mm.

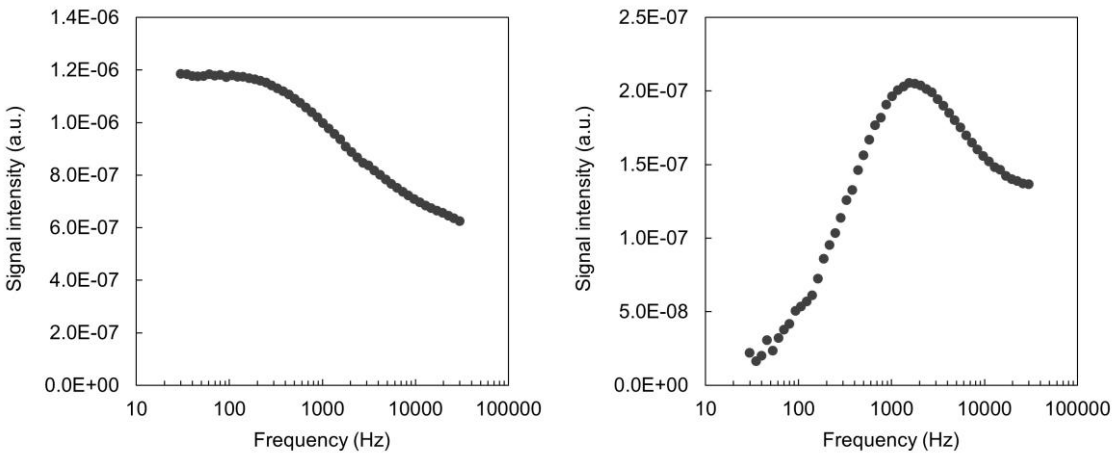

Figure 7. AC susceptibility spectrum of Resovist measured from 10 Hz to 10 kHz. (a) Real part of the susceptibility (χ') and (b) imaginary part of the susceptibility (χ''). Both χ' and χ'' retain non-negligible values at 500 Hz, indicating that nonlinear relaxation processes remain active and can generate measurable higher-order harmonics.

3.3 Cross-Sectional Imaging Using a Conical Spiral Sample

Similar to the system function measurement, we used Resovist® (FUJIFILM Toyama Chemical Co., Ltd.) as the MNP material. A conical spiral sample was fabricated by sealing the MNPs in the shape of a helical tube with the X-axis as the central axis. This sample was designed to mimic vascular structures for angiographic imaging evaluation. A conical spiral shape was adopted so that the MNP position in each Y–Z cross-section changes as a function of the X-position. Fig. 8 shows a three-dimensional model and an actual photograph of the sample.

In this measurement, the drive field was set to a frequency of 500 Hz and an amplitude of 19 mT, while the selection-field gradient was set to 1.5 T/m. The data were acquired under both Co-Config. and Ortho-Config. coil arrangements. The conical spiral sample was divided into seven X-slices corresponding to X = –40, –30, –20, –10, 0, 10, and 20 mm. For each X-slice, projection data were acquired by translating the sample along the Y-direction at 20 displacement positions and rotating it around the X-axis at 50 angular positions. The third-harmonic lock-in signal was recorded at each displacement and angular position to construct a sinogram for each X-slice.

For each X-slice, the MNP distribution in the Y–Z plane was reconstructed independently from the corresponding sinogram. Based on the system-function formulation introduced in Section 2.1, the measured voltage vector was represented by the product of the system-function matrix and the MNP distribution vector. The reconstruction was performed as a non-negative least-squares problem: $\hat{\boldsymbol{c}} = \underset{c\geq 0}{\operatorname{argmin}}\left\|\boldsymbol{S}\boldsymbol{c} - \boldsymbol{u}_{\mathrm{expt}}\right\|^2$. Here, $\boldsymbol{S}$ is the system-function matrix, $\boldsymbol{c}$ is the MNP distribution vector in

the Y–Z plane, and $\boldsymbol{u}_{\mathrm{expt}}$ is the measured third-harmonic voltage vector. No deconvolution, interpolation-based image generation, explicit regularization, or coupling between different X-slices was applied. The only constraint imposed in the reconstruction was the non-negativity of $\boldsymbol{c}$. Therefore, Figs. 11 and 12 represent slice-by-slice two-dimensional reconstructions of the MNP distribution in the Y–Z plane based on the third-harmonic sinograms.

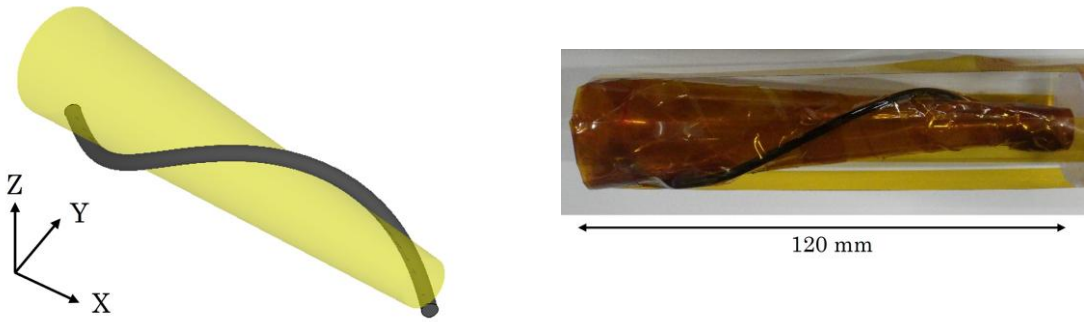

(a) Conical spiral sample 3D model (b) Actual sample

Figure 8. Conical spiral sample used for cross-sectional imaging: (a) 3D model and (b) actual sample photograph.

4. Results

4.1 One-Dimensional System Function

One-dimensional system functions were measured along the X- and Y-directions for both Co-Config. and Ortho-Config. The experimental profiles and the corresponding theoretical curves are shown in Figs. 9 and 10. The theoretical curves were calculated under the same gradient and drive-field conditions as the experiments and were overlaid on the measured profiles.

In Co-Config., the measured profiles showed a single-polarity response along both the X- and Y-directions. The corresponding theoretical curves exhibited the same tendency, showing single-peak profiles without polarity inversion. This behavior reflects the spatial symmetry of the system function when the drive-field direction is aligned with the FFL direction.

In Ortho-Config., the profiles showed a different spatial pattern. Along the X-direction, the measured profiles exhibited polarity inversion and oscillatory features around the FFL. The theoretical curves also showed sign-changing profiles in the X-direction, indicating that this behavior arises from the position-dependent time-derivative component of the effective magnetic field. This behavior is consistent with the numerical system-function maps in Figs. 2 and 3, where Ortho-Config. exhibits sharper spatial variation together with polarity reversal, rather than a simple narrowing of a single-polarity profile. Along the Y-direction, both the measured and theoretical profiles showed a single-

peak response without pronounced polarity inversion.

In both configurations, the signal amplitude decreased with increasing harmonic order from the third to the seventh harmonic. The profiles also showed sharper spatial variation for higher harmonic orders and for larger selection-field gradients. These tendencies were observed in both experimental and theoretical profiles.

The theoretical curves reproduced the main spatial features of the measured profiles, including the single-polarity response in Co-Config. and the sign-changing response in Ortho-Config. However, the measured profiles were broader than the theoretical curves, particularly along the X-direction. This difference can be attributed to practical factors not fully included in the simplified theoretical model, such as the finite size of the cylindrical sample, the nonideal selection-field distribution generated by the permanent magnets and iron yokes, the finite low-field region around the FFL, and the spatial sensitivity distribution of the gradiometer receive coil.

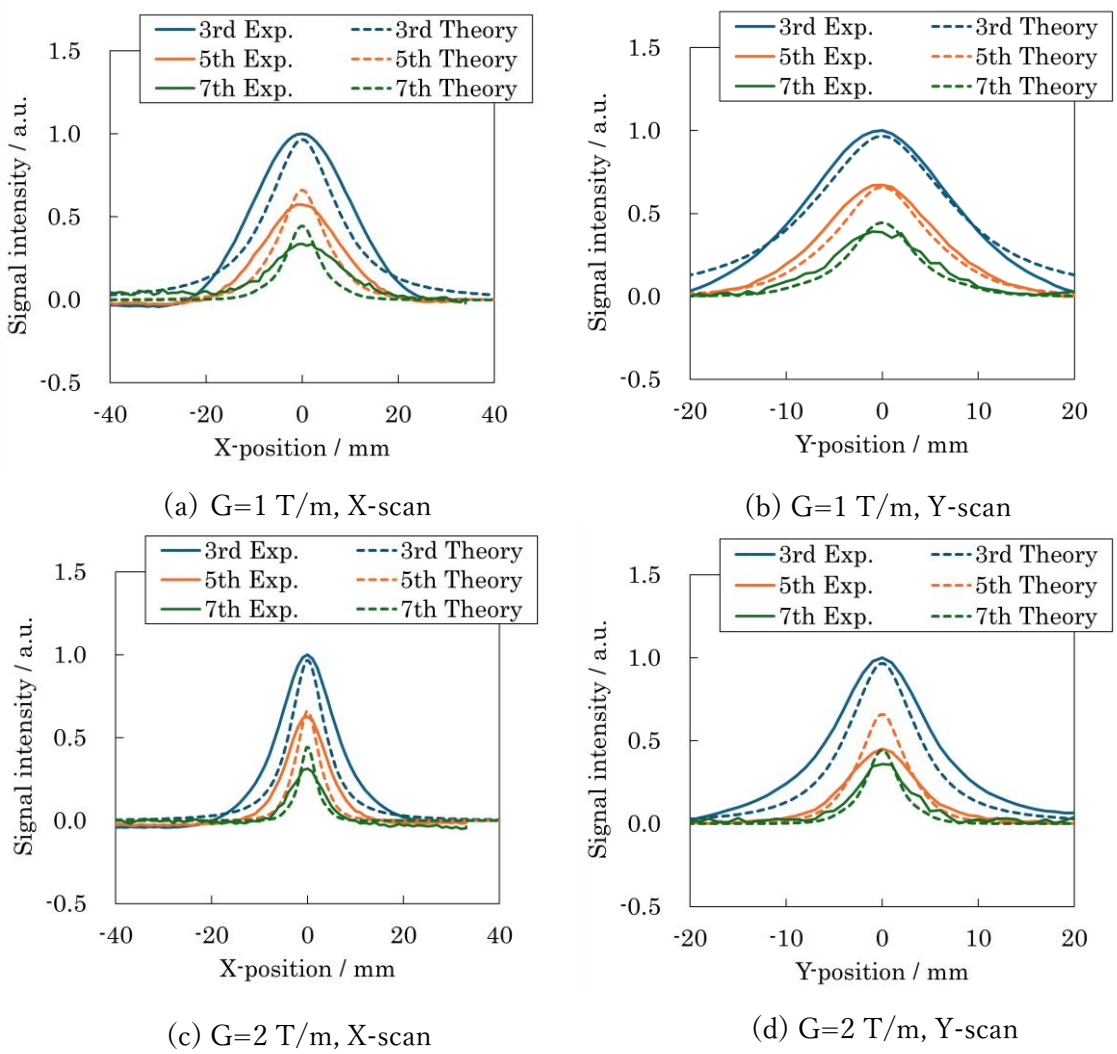

Figure 9. One-dimensional profiles of the experimentally measured and theoretically calculated system functions from the third to seventh harmonic signals in Co-Config.: (a) X-direction (Y = 0) profile for G = 1 T/m; (b) Y-direction (X = 0) profile for G = 1 T/m; (c) X-direction (Y = 0) profile for G = 2 T/m; and (d) Y-direction (X = 0) profile for G = 2 T/m. Solid and dashed lines indicate the experimental and theoretical profiles, respectively.

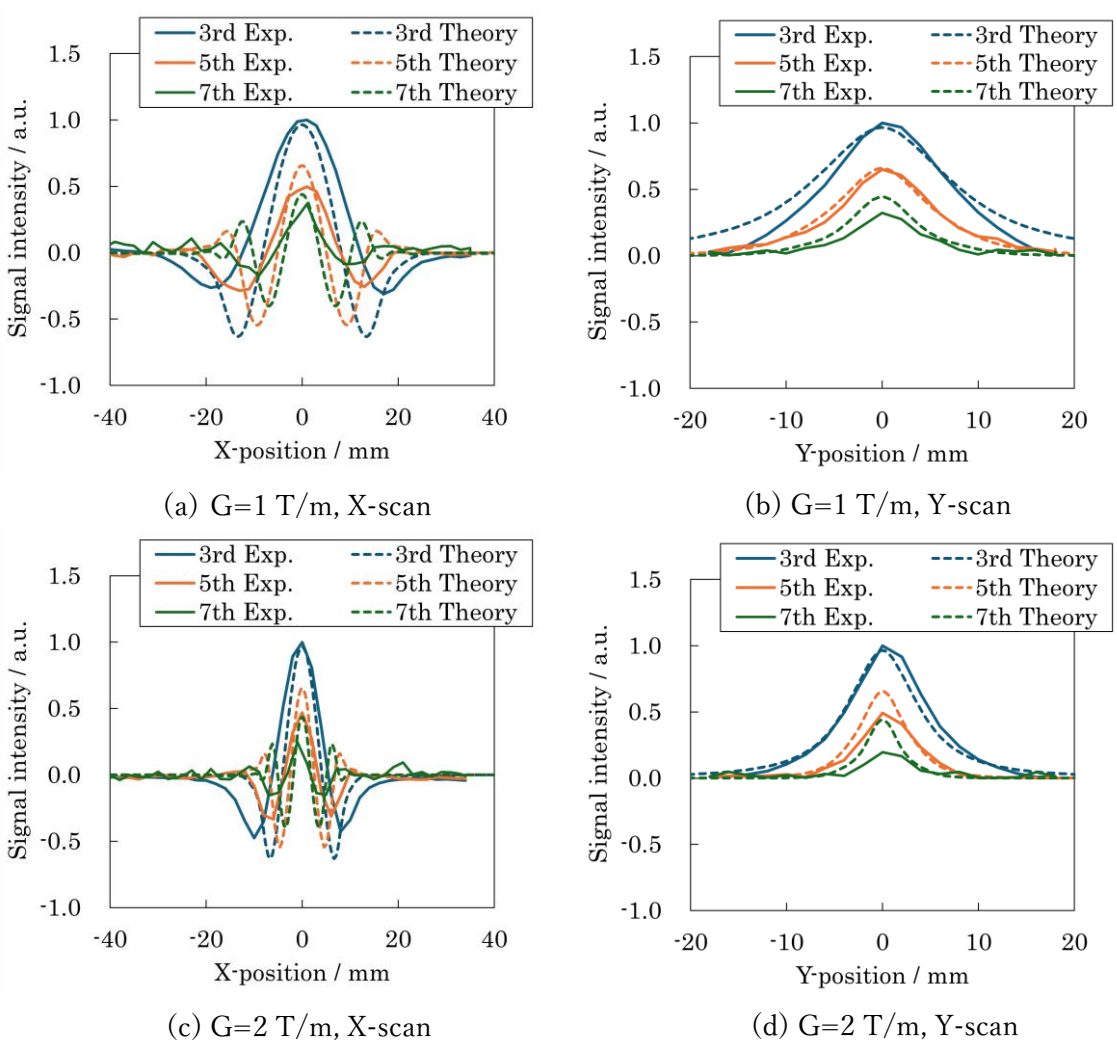

Figure 10. One-dimensional profiles of the experimentally measured and theoretically calculated system functions from the third to seventh harmonic signals in Ortho-Config.: (a) X-direction (Y = 0) profile for G = 1 T/m; (b) Y-direction (X = 0) profile for G = 1 T/m; (c) X-direction (Y = 0) profile for G = 2 T/m; and (d) Y-direction (X = 0) profile for G = 2 T/m. Solid and dashed lines indicate the experimental and theoretical profiles, respectively.

4.2 Cross-Sectional Imaging of the Conical Spiral Sample

Subsequently, we performed cross-sectional imaging of the conical spiral sample using both Co-Config. and Ortho-Config. and evaluated how the system function influences the reconstructed response. Figs. 11 and 12 show the reconstructed Y–Z distributions at seven X-slice positions for each configuration. As described in Section 3.3, these images were obtained by slice-by-slice two-dimensional non-negative least-squares reconstruction from third-harmonic sinograms acquired by Y-

direction translation and rotation around the X-axis.

In Co-Config., the signal distribution was reconstructed at each X-slice position along the conical spiral sample. As the X-position varied, the reconstructed MNP distribution changed its position in the Y–Z plane, reflecting the helical geometry of the sample. The reconstructed images showed relatively continuous signal distributions across the X-slices.

In Ortho-Config., the reconstructed distributions also followed the conical spiral geometry, but localized reductions in effective signal amplitude were observed in some slices. These reductions are related to the sign-changing sensitivity profile of the system function in Ortho-Config., which can cause partial cancellation of opposite-polarity signal components under the present third-harmonic, slice-by-slice reconstruction condition. This result should not be interpreted as a general limitation of Ortho-Config. Rather, it indicates that the sign-changing system function must be explicitly incorporated when interpreting or reconstructing the measured signal. In a more complete reconstruction framework that uses the full system function, including multi-harmonic information and three-dimensional coupling, the sharper spatial variation in Ortho-Config. may provide additional spatial-encoding

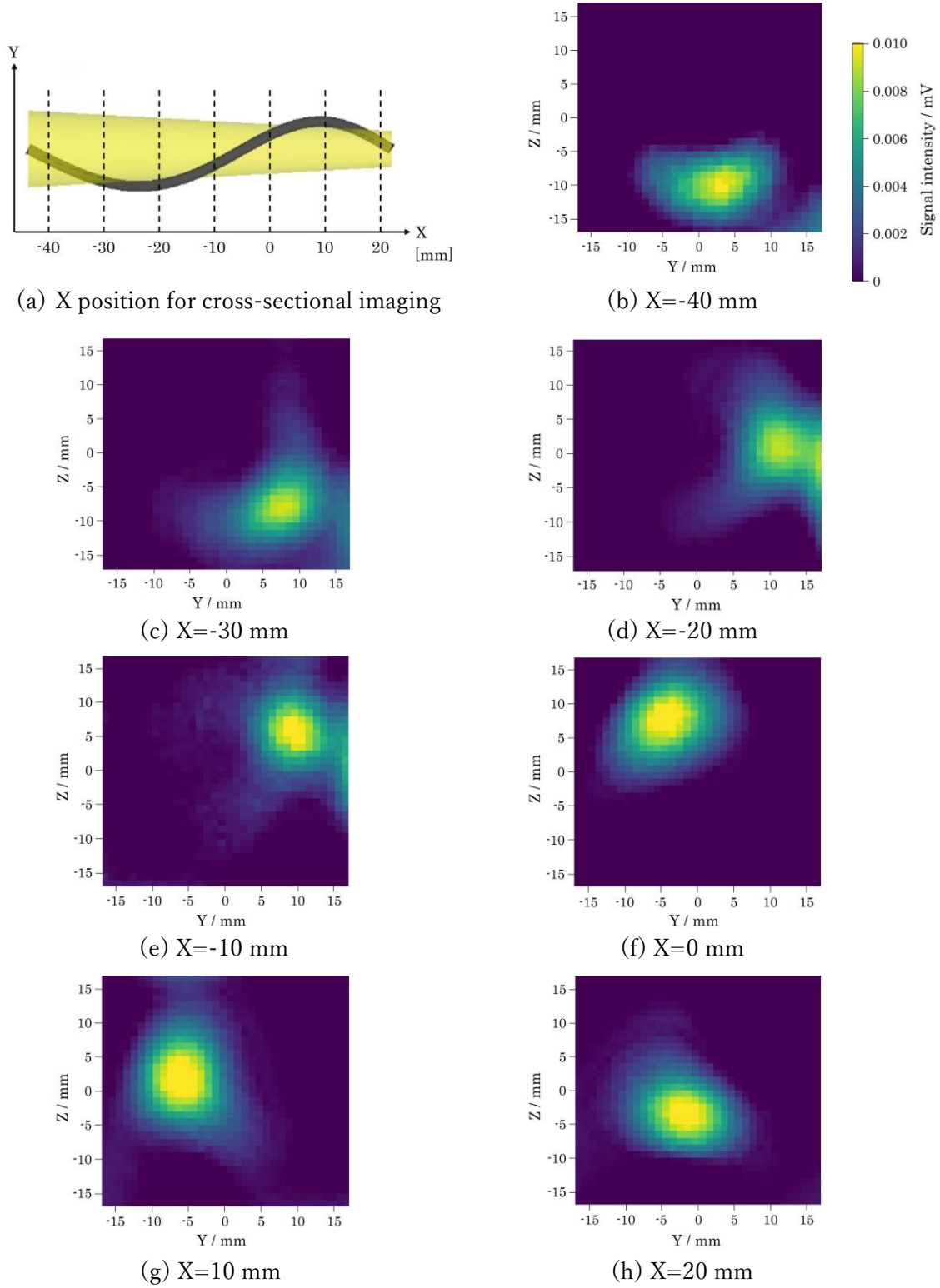

(a) X position for cross-sectional imaging

(b) X=-40 mm

(c) X=-30 mm

(d) X=-20 mm

(e) X=-10 mm

(f) X=0 mm

(g) X=10 mm

(h) X=20 mm

Figure 11. Cross-sectional imaging (Y-Z plane) of the conical spiral sample in Co-Config. using the third harmonic signal (k = 3): X = –40, –30, –20, –10, 0, 10, 20 mm, with A = 16 mT and G = 1.5 T/m.

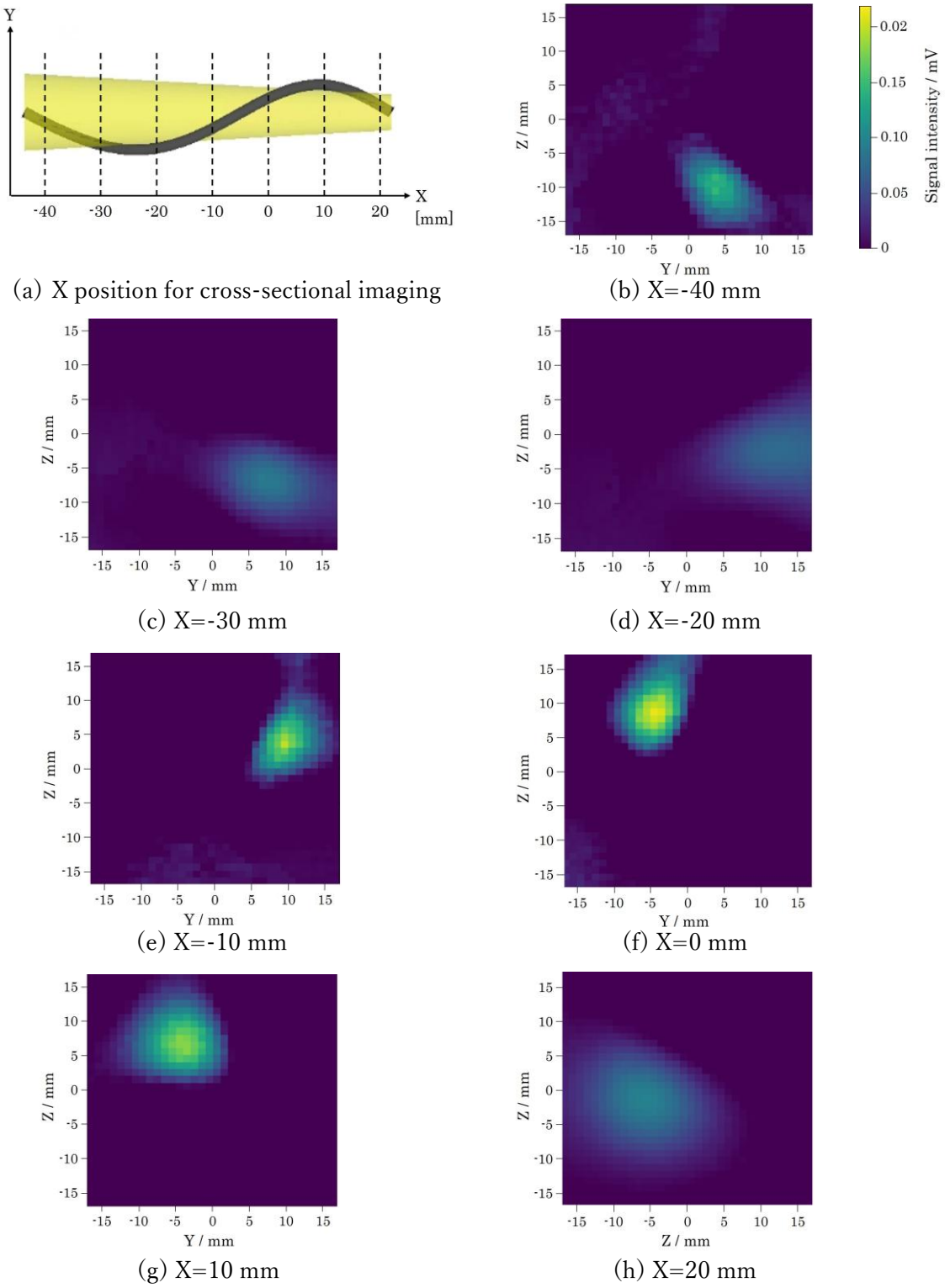

(a) X position for cross-sectional imaging

(b) X=-40 mm

(c) X=-30 mm

(d) X=-20 mm

(e) X=-10 mm

(f) X=0 mm

(g) X=10 mm

(h) X=20 mm

Figure 12. Cross-sectional imaging (Y-Z plane) of the conical spiral sample in Ortho-Config. using the third harmonic signal (k = 3): X = –40, –30, –20, –10, 0, 10, 20 mm, with A = 16 mT and G = 1.5 T/m.

5. Discussion

The results obtained in this study indicate that the relative orientation between the FFL and the drive field strongly affects the native system function in FFL-based MPI. In Co-Config., the system function showed a single-polarity response under the present measurement conditions. In Ortho-Config., the system function exhibited sharper spatial variation together with polarity inversion. Under the third-harmonic acquisition and slice-by-slice reconstruction procedure used in this study, this polarity inversion caused partial cancellation of opposite-polarity signal components and localized reductions in reconstructed signal amplitude.

These conclusions are limited to the present single-harmonic acquisition and slice-by-slice reconstruction framework. The results should not be interpreted as indicating a general disadvantage of Ortho-Config. The sharper spatial variation and polarity inversion observed in Ortho-Config. may provide high-spatial-frequency encoding information when the full system function is explicitly incorporated into a more complete reconstruction framework. Future work should therefore evaluate both configurations using multi-harmonic acquisition, system-matrix reconstruction, and three-dimensional reconstruction models. The present study provides a controlled comparison of the native system-function characteristics of the two coil geometries under matched drive-field and selection-field conditions.

Several strategies for generating an FFL have been reported in the MPI literature, including electromagnetically generated FFLs using gradient coils, electronically rotated FFLs, single-sided FFL generators, mechanically scanned FFL generators, and hybrid approaches combining permanent magnets and coils [12], [14], [17]-[20], [28]. The FFL used in our experiments belongs to the permanent-magnet-based category, which offers stable gradient fields without power consumption and simplifies system implementation. Positioning our configuration within this broader set of techniques clarifies its relationship to representative FFL formation strategies.

Regarding practical implementation, the scalability of the two configurations differed considerably. The long solenoidal drive coil used in our prototype Co-Config. is not intended for human-scale systems. Alternative geometries such as Helmholtz or birdcage-type coils may be adopted to relax geometric constraints. Recent studies have also demonstrated the electronic steering of the FFL and multichannel receiver arrays to reduce the need for mechanical rotation. In contrast, Ortho-Config. has been implemented in several bench-top and preclinical MPI systems, making it structurally easier to scale toward larger scanners. These considerations indicate that while Co-Config. provides uniform polarity and simplified detection, Ortho-Config. may offer greater feasibility for large-volume or human-scale imaging.

The cross-sectional response maps obtained using the conical spiral sample should also be interpreted within the scope of the present acquisition method. The present imaging experiment used planar imaging with a fixed FFL, and the measured signal was integrated along the FFL direction. Therefore,

the images shown here are intended to compare coil-geometry-dependent spatial responses under identical acquisition conditions, rather than to demonstrate full tomographic reconstruction performance.

The homogeneity of the FOV should also be considered when interpreting the conical-spiral phantom results. The analytical selection-field model assumes a linear FFL near the central region of the scanner, whereas the actual field generated by permanent magnets and U-shaped yokes inevitably deviates from an ideal linear field toward the edges of the FOV. Therefore, the FFL is expected to be most linear near the central region and less ideal near the outer slices of the spiral phantom. In Ortho-Config., the drive field also shifts the low-field region along the X-direction. Under the imaging condition used in this study, the nominal drive-induced displacement estimated from the drive-field amplitude and selection-field gradient was approximately 13 mm. This displacement was within the central region of the drive coil, but residual drive-field inhomogeneity, nonideal selection-field linearity, finite FFL width, and receive-coil sensitivity variation can contribute to broadening and slice-dependent intensity variations in the reconstructed images. Reconstruction in the X–Z plane, or full three-dimensional reconstruction, would require a reconstruction model that explicitly includes the X-dependent system function and coupling between neighboring X-slices. Thus, the present Y–Z slice-by-slice images should be interpreted as a controlled comparison of coil-geometry-dependent spatial responses, rather than as a quantitative evaluation of homogeneous-FOV tomographic performance.

6. Conclusion

This study presented a comparative analysis of the system-function characteristics in an FFL-based MPI for two coil geometries: Co-Config. and Ortho-Config. In Co-Config., the selection and drive fields were aligned, resulting in consistent polarity in the time-derivative field component and the absence of polarity inversion. In Ortho-Config., the fields were perpendicular, resulting in spatially dependent sign changes due to nonlinear field superposition. Numerical simulations and experimental measurements demonstrated that Co-Config. provides a uniform system function suitable for single-harmonic reconstruction, while Ortho-Config. exhibits sharper spatial variation together with polarity inversion, which can be more appropriately handled by multi-harmonic or system–matrix reconstruction.

Cross-sectional imaging using a conical spiral sample further showed that Co-Config. yields a stable reproduction of the nanoparticle distribution, while Ortho-Config. exhibited localized contrast reductions corresponding to sign-changing regions in the selected harmonic component. Although modern reconstruction frameworks can compensate for these regions, the underlying system function still influences the stability and interpretation of single-harmonic reconstruction, highlighting coil geometry as a key design parameter.

Rather than identifying a universally optimal coil configuration, this study clarifies the hardware-level

trade-offs between Co-Config. and Ortho-Config. The findings provide practical design considerations under specific constraints related to native spatial encoding characteristics, reconstruction strategy, and system implementation, and contribute to a deeper understanding of FFL-MPI. These insights will be useful for the future development of scalable MPI hardware systems for clinical and preclinical applications.

Fundings

This research was supported by the Advanced Measurement and Analysis Technology and Instrument Development Program of the Japan Agency for Medical Research and Development (AMED) under Grant Number JP19hm0102073.

Acknowledgements

The authors would like to thank the members of the research teams at Mitsubishi Electric, Osaka University, and Okayama University for their valuable discussions and technical support.

Author contributions

M.W. conceived and designed the study, conducted the experiments, and wrote the manuscript.
T.M. contributed to the development of the imaging systems.
C.L. supported the numerical modeling, theoretical analysis, and image reconstruction.
S.S. and T.N. designed the imaging experiments and interpreted the data.
T.K. provided scientific supervision and contributed to the data interpretation.
All the authors discussed the results and contributed to the final version of the manuscript.

Competing interests

C.L. is the co-inventor on a patent application related to this work:
"MAGNETIC FIELD GENERATION DEVICE, IMAGING DEVICE, AND MAGNETIC FIELD GENERATION METHOD," WO2023/047761, filed by Mitsubishi Electric Corporation (published March 30, 2023).
All other authors declare no competing interests.

Data Availability

The datasets generated and analysed during the current study are available from the corresponding author on reasonable request.

References

[1] Bernhard Gleich and Jürgen Weizenecker, "Tomographic Imaging Using the Nonlinear Response of Magnetic Particles," *Nature*, **435**(7046), 1214–1217 (2005).

[2] Patrick W Goodwill and Steven M Conolly, "Multidimensional X-Space Magnetic Particle Imaging," *IEEE Transactions on Medical Imaging*, **30**(9), 1581–1590 (2011).

[3] L. C. Wu, Y. Zhang, G. Steinberg, H. Qu, S. Huang, M. Cheng, T. Bliss, F. Du, J. Rao, G. Song, L. Pisani, T. Doyle, S. Conolly, K. Krishnan, G. Grant, and M. Wintermark, "A Review of Magnetic Particle Imaging and Perspectives on Neuroimaging," *American Journal of Neuroradiology*, **40**(2), 206–212 (2019).

[4] C. Billings, M. Langley, G. Warrington, F. Mashali, and J. A. Johnson, "Magnetic Particle Imaging: Current and Future Applications, Magnetic Nanoparticle Synthesis Methods and Safety Measures," *International Journal of Molecular Sciences*, **22**(14), 7651 (2021).

[5] B. Rezaei, Z. W. Tay, S. Mostufa, O. N. Manzari, E. Azizi, S. Ciannella, H.-E. J. Moni, C. Li, M. Zeng, J. Gómez-Pastora, and K. Wu, "Magnetic Nanoparticles for Magnetic Particle Imaging (MPI): Design and Applications," *Nanoscale*, 16, 11802–11824 (2024).

[6] Zhi Wei Tay, Prashant Chandrasekharan, Benjamin D. Fellows, Irati Rodrigo Arrizabalaga, Elaine Yu, Malini Olivo and Steven M. Conolly, "Magnetic Particle Imaging: An Emerging Modality with Prospects in Diagnosis, Targeting and Therapy of Cancer," *Cancers*, **13**(21), 5285 (2021).

[7] Elaine Y. Yu, Mindy Bishop, Bo Zheng, R. Matthew Ferguson, Amit P. Khandhar, Scott J. Kemp, Kannan M. Krishnan, Patrick W. Goodwill and Steven M. Conolly, "Magnetic Particle Imaging: A Novel In Vivo Imaging Platform for Cancer Detection," *Nano Letters*, **17**(3), 1648–1654 (2017).

[8] X. Y. Zhou, Z. W. Tay, P. Chandrasekharan, E. Y. Yu, D. W. Hensley, R. Orendorff, K. E. Jeffris, D. Mai, B. Zheng, P. W. Goodwill, and S. M. Conolly, "Magnetic Particle Imaging for Radiation-Free, Sensitive and High-Contrast Vascular Imaging and Cell Tracking," Current Opinion in Chemical Biology, 45, 131–138 (2018).

[9] J. Weizenecker, B. Gleich, J. Rahmer, H. Dahnke, and J. Borgert, "Three-dimensional Real-time In Vivo Magnetic Particle Imaging," *Physics in Medicine & Biology*, **54**(5), L1–L10 (2009).

[10] Svetlana Konnova and Elvira Rozhina, "Magnetic Nanoparticles for Biomedical and Imaging Applications," *International Journal of Molecular Sciences*, **25**(11), 5847 (2024).

[11] Tobias Knopp and Thorsten M. Buzug, "Magnetic Particle Imaging: An Introduction to Imaging Principles and Scanner Instrumentation," *Springer*, 2012.

[12] P. W. Goodwill, J. J. Konkle, B. Zheng, E. U. Saritas, and S. M. Conolly, "Projection X-

Space Magnetic Particle Imaging," IEEE Transactions on Medical Imaging, 31(5), 1076–1085 (2012).

[13] Serhat Ilbey, Can Barıs Topa, Alper Güngöra, Tolga Çukur, Emine Ulku Saritas and Hüseyin Emre Güvena, "Comparison of System-Matrix-Based and Projection-Based Reconstructions for Field Free Line Magnetic Particle Imaging," *International Journal on Magnetic Particle Imaging*, **3**(1), 1703022 (2017)

[14] Tobias Knopp, Marlitt Erbe, Sven Biederer, Timo F. Sattel and Thorsten M. Buzug, "Efficient Generation of a Magnetic Field-Free Line," *Medical Physics*, **37**(7), 3538–3540 (2010).

[15] Can Barıs and Alper Güngör, "Tomographic Field Free Line Magnetic Particle Imaging With an Open-Sided Scanner Configuration," *IEEE Transactions on Medical Imaging*, **39**(12), 4164–4173 (2020).

[16] J. J. Konkle, P. W. Goodwill, O. M. Carrasco-Zevallos, and S. M. Conolly, "Projection Reconstruction Magnetic Particle Imaging," *IEEE Transactions on Medical Imaging*, **32**(2), 338–347 (2013).

[17] K. Bente, M. Weber, M. Graeser, T. F. Sattel, M. Erbe, and T. M. Buzug, "Electronic Field Free Line Rotation and Relaxation Deconvolution in Magnetic Particle Imaging," *IEEE Transactions on Medical Imaging*, **34**(2), 644–651 (2015).

[18] Jason Pagan, Chris McDonough, Triet Vo and Alexey Tonyushkin, "Single-Sided Magnetic Particle Imaging Device with Field-Free-Line Geometry for In Vivo Imaging Applications," *IEEE Transactions on Magnetics*, **57**(2), 5300105 (2021).

[19] A. Tonyushkin, "Single-Sided Field-Free Line Generator Magnet for Multidimensional Magnetic Particle Imaging," *IEEE Transactions on Magnetics*, **53**(9), 5300506 (2017).

[20] Chris McDonough and Alexey Tonyushkin, "1D Imaging with a Single-Sided FFL Magnetic Particle Imaging Scanner," *International Journal on Magnetic Particle Imaging*, **8**(1 Suppl 1), 2203033 (2022).

[21] Masaomi Washino, Kota Nomura, Kazuki Yamauchi, Tetsuya Matsuda, Yasuaki Susumu, Satoshi Seino, Takashi Nakagawa, Toshiyasu Sakane, Toshihiko Kiwa, Shun Tonooka, "Magnetic Signal Evaluation and Imaging of Magnetic Nanoparticles in Brain Phantom," *International Journal on Magnetic Particle Imaging*, **8**(1), Suppl 1, (2022).

[22] Kota Nomura, Masaomi Washino, Tetsuya Matsuda, Satoshi Seino, Takashi Nakagawa, Toshihiko Kiwa, Makoto Kanemaru, "Development of Human Head Size Magnetic Particle Imaging System," *International Journal on Magnetic Particle Imaging*, **10**(1), Suppl 1, Article ID 2403001, (2024).

[23] Satoshi Seino, Hiroto Ikehata, Mizuki Tanabe, Tomohiro Umeda, Takami Tomiyama, Akiko Tanaka, Tomoyuki Furubayashi, Toshiyasu Sakane, Toshihiko Kiwa, Masaomi

Washino, Kota Nomura, Shun Tonooka, Akihiro Izawa, Yuki Okumura, Takashi Nakagawa, "Investigating the Efficacy of Nasal Administration for Delivering Magnetic Nanoparticles into the Brain for Magnetic Particle Imaging," *Journal of Controlled Release*, **367**, 515-521 (2024).

[24] Liwen Zhang, Yusong Shen, Fan Yang, Hui Yukong, Jie Tian, "MPI Reconstruction Based on System Matrix Using a Field Free Line," *International Journal on Magnetic Particle Imaging*, **9**(1), Suppl 1, 2303007 (2023).

[25] Vladyslav Gapyak, Thomas März, Andreas Weinmann, "Reconstruction Formulae for 3D Field-Free Line Magnetic Particle Imaging," *arXiv preprint*, arXiv:2309.06254 (2023).

[26] Fabian Mohn, Tobias Knopp, Marija Boberg, Florian Thieben, Patryk Szwargulski, Matthias Graeser, "System Matrix Based Reconstruction for Pulsed Sequences in Magnetic Particle Imaging," *IEEE Transactions on Medical Imaging*, 41(7), 1862–1871 (2022).

[27] Ivo Matteo Baltruschat, Patryk Szwargulski, Florian Griese, Mirco Grosser, René Werner, Tobias Knopp, "3D-SMRnet: Achieving a New Quality of MPI System Matrix Recovery by Deep Learning," *arXiv preprint*, arXiv:1905.03026 (2019).

[28] Tae Yi Kim, Jae Chan Jeong, Beom Su Seo, Hans Joachim Krause, and Hyo Bong Hong, "A Novel Field-Free Line Generator for Mechanically Scanned Magnetic Particle Imaging," *Sensors*, **24**(3), 933 (2024).